JOURNAL OF MATERIALS SCIENCE 22 (1987) 1120–1126

On the plastic deformation of fibre self-reinforced polymers

J. PETERMANN, U. RIECK
Polymer and Composites Group, Technical University of Hamburg–Harburg, Harburger Schlossstrasse 20, 2100 Hamburg 90, West Germany

The plastic deformation of semi-crystalline polymers containing needle crystals has been investigated. Stress–strain curves exhibit two linear regions, the elastic (Hookeian) range and a second linear plastic part. The onset of the plastic part depends on pre-straining and the slope $\alpha = d\sigma/d\varepsilon$ of the plastic part is dependent on the morphology of the samples. An interpretation is given in terms of the shear-lag theory of discontinuous uniaxially oriented fibres.

1. Introduction

Melt-processed thermoplastic semi-crystalline polymers exhibit under normal processing conditions a lamellar morphology of the crystalline phase. But if crystallization occurs under extremely high extensional flow conditions of the melt a needle-crystalline morphology can arise [1–4]. In this morphology the crystallites have the shape of tiny fibres being about 100 nm long with a diameter of only approximately 10 nm. The length of the fibres is dependent on processing conditions (temperature, flow gradient) [5] and on the polymer, and can vary over several orders of magnitude while the diameter does not change significantly [6]. The needle crystals are embedded in the amorphous matrix of the same polymer. The macromolecules of the amorphous matrix are non-oriented. The overall morphology of this material has a strong resemblance to unidirectional discontinuous-fibre reinforced composites. Recently it has been demonstrated that the elastic properties (Young's modulus, E) of the needle crystalline materials follow the rules of fibre-reinforced composite theory (FRCT) [7]. It is the purpose of this paper to investigate the plastic part of deformation and to compare it with that of fibre-reinforced composites.

2. Experimental details

2.1. Sample preparation

The materials used in the present work were polybutene-1 (PB-1, M_W = 800 000) and polyethyleneterephthalate (PET, M_W = 90 000). The samples were prepared according to the method of Petermann and Gohil [8] (Fig. 1).

A small amount of the polymer solution (1% PB-1 in xylene and 0.4% PET in trifluoroacetic acid) was poured onto a hot glass plate. After the solvents had evaporated the remaining thin polymer film was picked up on a motor-driven cylinder which allowed one to wind up about 1000 layers in order to obtain thick (100 μm) samples for the mechanical tests. Electron-transmissible films were obtained by using single layers which were cut into small pieces, floated off on distilled water and finally put on to copper grids. The thick specimens were dried in an oven at 50° C and then pressed at room temperature (RT) at a pressure of 220 bar (22 MPa). While the PET samples were annealed at different temperatures (with fixed ends) with the aim to vary the morphology, the PB-1 samples did not experience any further heat treatment because the needle length was varied by different drawing temperatures. Amorphous PET foils were produced by melting the granulate in a hot press at 280° C and 100 bar (10 MPa) for 5 min and subsequent quenching in ice-water.

The sample preparations described above lead to the following different morphologies:

(i) short-needle PB-1 films;
(ii) long-needle PB-1 films;
(iii) micellar PET
(iv) lamellar PET;
(v) amorphous PET.

2.2. Characterization techniques

Transmission electron microscopy was used to determine the morphological structure of the polymers. They were examined in a Philips EM 400 T, operated at 100 kV, using bright-field and diffraction techniques.

The mechanical tests were carried out with a Zwick 1445 tensile testing machine using deformation velocities of 1 mm min^{-1} for the PB-1 and 5 mm min^{-1} for the PET samples. The specimen size was 50 mm × 6 mm, gauge length 35 mm. The testing temperature was kept below the glass transition temperature of the

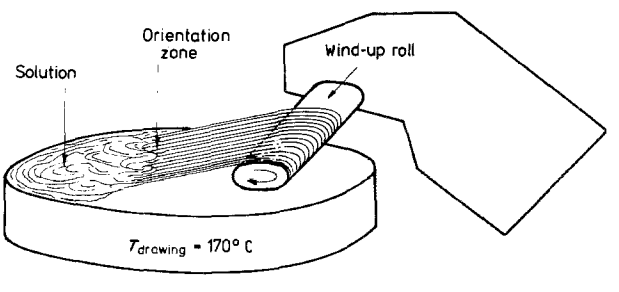

Figure 1 Schematic sketch of the film-spinning apparatus.

0022–2461/87 $03.00 + .12

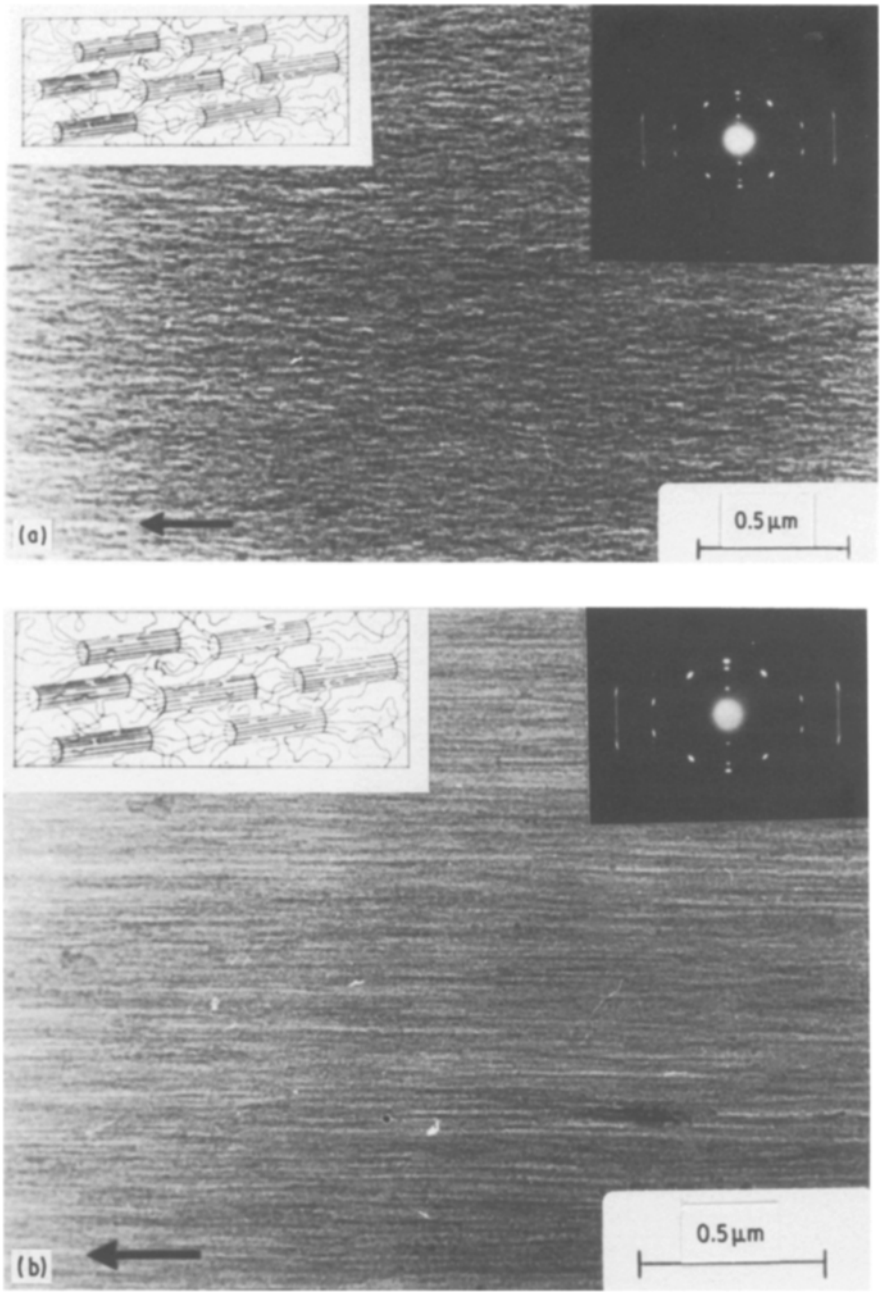

Figure 2 Bright-field transmission electron micrograph of needle crystalline PB-1. Inserted is the corresponding electron diffraction as well as a sketch of the morphology: (a) drawn at 100° C, (b) drawn at 150° C. Arrows denote the *c* direction.

matrices (PB-1; T_g − 10° C, PET: T_g = 70° C) at − 50 and + 20° C, respectively.

3. Results

3.1. Crystalline morphologies

Fig. 2 shows TEM micrographs of the morphology of the PB-1 samples (schematic sketches are inserted) drawn from the melt at 100 and 150° C, respectively. In the case of the lower preparation temperature the average needle length $\bar{l}$, is about 100 nm (Fig. 2a) whereas the needle length increases to about 370 nm at a preparation temperature of 150° C (Fig. 2b) [9]. As can be seen from the micrographs the samples are highly oriented, with well-aligned needle crystals in the orientation direction. The crystalline morphologies of melt-spun PET samples are shown in TEM micrographs (Fig. 3). In the as-drawn state the material consists of single micelles which are preferentially aligned in the orientation direction (Fig. 3a) as can be seen from the inserted diffraction pattern. Annealing at 200° C causes a morphological transformation into lamellae-like crystals which are formed by lateral crystallization (Fig. 3b) [10].

3.2. Cyclic deformation

The general deformation behaviour of the samples characterized as described above is illustrated in Fig. 4. Two linear regions in the deformation curve can be recognized. The stress–strain curves shown in Fig. 5 are from the cyclic deformation of PB-1 samples with average needle length of 100 nm (Fig. 5a) and 370 nm (Fig. 5b). The first cycle does not exceed the Hookeian range, as can be seen from the 100% reversibility after unloading the samples. Straining the second time results in a linear elastic part followed by a second linear part with a slope $\alpha = d\sigma/d\varepsilon$. Comparing Fig. 5a with Fig. 5b a strong increase in α as well as Young's modulus, E, with increasing needle length can be detected. Following the number n of deformation cycles, E and α remain nearly constant. Table I shows the values of E and α for the two different needle lengths. Similar deformation behaviour is

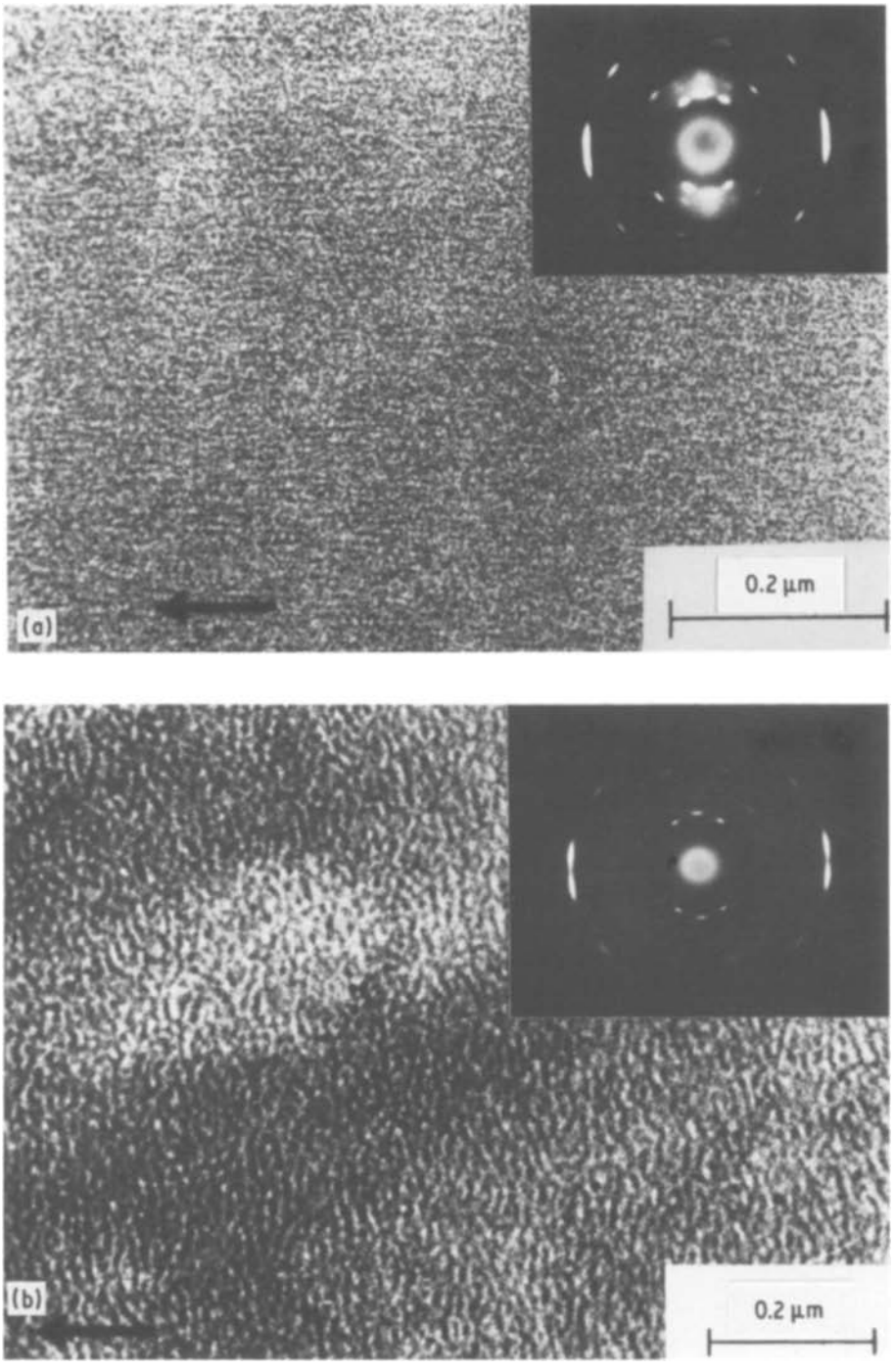

Figure 3 Phase contrast electron micrograph of drawn PET (diffraction pattern is inserted, arrows denote the *c* direction): (a) as-drawn, (b) annealed at 200° C.

observed when straining as-drawn and 200° C annealed PET, as can be seen from Figs 6a and b. In the first case (micellar morphology, Fig. 6a) again a second linear part follows the Hookeian range with a slope which is well below the value of α, obtained from PB-1 samples (see Table I). Again the modulus, E, does not change with increasing cycles, n. No second linear part (at higher strains) occurs when the 200° C annealed PET samples are stretched (Fig. 6b), although the Young's modulus has increased considerably. Obviously this fact is caused by the change in morphology from micellar to lamellar. Deformation curves of amorphous PET are shown in Fig. 6c. After the Hookeian range necking occurs.

TABLE I Experimental values for Young's modulus and its dependence on sample morphology

Polymer	Morphology*	Deformation temperature (° C)	Young's modulus (GPa)	$d\sigma/d\varepsilon$ (MPa)
PB-1	Needle-like, $\bar{l}$ = 100 nm	−50	3.3	1010
PB-1	Needle-like, $\bar{l}$ = 370 nm	−50	5.85	2460
PET	Micellar	RT	1.42	205
PET	Lamellar	RT	3.2	–
PET	Amorphous	RT	1.22	–

*$\bar{l}$ = average needle length.

4. Discussion

Similar stress–strain curves with two different regions have been obtained in uniaxially oriented fibre composites for tungsten fibres in a copper matrix [11] and for Al_2O_3 fibres in an epoxide matrix [12]. In the case of continuous tungsten fibres in the copper matrix, two different slopes in the stress–strain curves occur

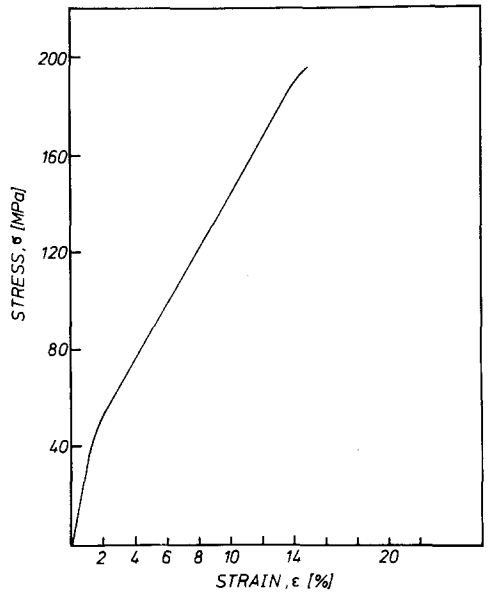

Figure 4 Stress–strain curve of PB-1, drawn at 100° C.

resulting from the rule of mixtures:

$$E_c = v_f E_f + (1 - v_f) E_m$$

where in the elastic part E_m denotes the Young's modulus of the matrix, v_f the volume fraction of the fibres, and E_f the Young's modulus of the fibres. As soon as the matrix deforms plastically, E_m has to be replaced by the work-hardening coefficient of the matrix,

$$\alpha = d\sigma/d\varepsilon$$

and if the work-hardening coefficient is independent of the strain, ε, two linear regions in the stress–strain curves of the composites are expected. With short-fibre reinforced composites [13] similar stress–strain curves can also result. The same arguments as mentioned for continuous-fibre composites may apply but additionally, two mechanisms can lead to deformation curves of these composites with two distinct regions: depending on the aspect ratio of the discontinuous fibres, the fibres can break after the composite has exceeded a limited strain [14] or the matrix can fail at the fibre ends [15] giving a decrease of the elastic slope as the strain increases.

As seen from the electron micrographs (Figs 2a and b and 3a) and the dependence of the Young's modulus on needle-crystal length, our material resembles very closely a short-fibre composite material with a broad distribution of needle crystal length (and aspect ratio) and an excellent bonding between fibres and matrix, as both consist of the same polymer being connected by tie-molecules. But none of the arguments mentioned above can account for the occurrence of stress–strain curves with two different linear slopes and the increase in strain of the first region (linear elastic part) with increasing numbers of cycles. A work-hardening of the matrix is not to be expected and not observed (Fig. 6c) and a failure of the matrix at the fibre ends or a breaking of the fibres has not been detected. A model for the mechanical behaviour of our material has to explain the following experimental results:

(i) the increase in yield stress with increasing number of cycles, and

(ii) the increase of the slope in the second linear part (plastic part) of the deformation curves with increasing needle length.

The assumptions for our model are a very broad distribution of the uniaxially oriented needle crystals and validity of the shear-lag model [16]. Let us suppose that we have a very short needle crystal (short means much smaller than l_c) in the vicinity of the end of a long needle crystal (long means much longer than $2l_c$) (Fig. 7). The shear stress distribution along the longer needle crystal with the strain of the overall material as parameter is shown in Fig. 8, as calculated from shear-lag theory:

$$\tau = E_f \varepsilon \left[\frac{G_m}{2E_f \ln (R/r_0)}\right]^{1/2} \frac{\sinh [\beta(l/2 - x)}{\cosh (\beta l/2)} \quad (1)$$

$$\beta = \left[\frac{G_m 2\pi}{E_f A_f \ln (R/r_0)}\right]^{1/2} \quad (2)$$

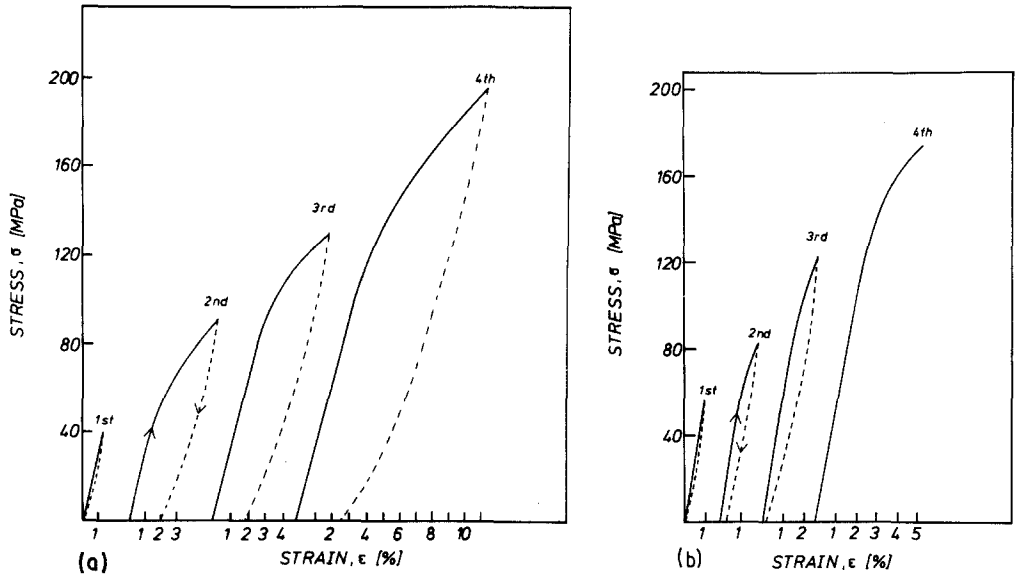

Figure 5 (a) Cyclic stress–strain curves of PB-1 (drawn at 100° C), (b) cyclic stress–strain curve of PB-1 (drawn at 150° C).

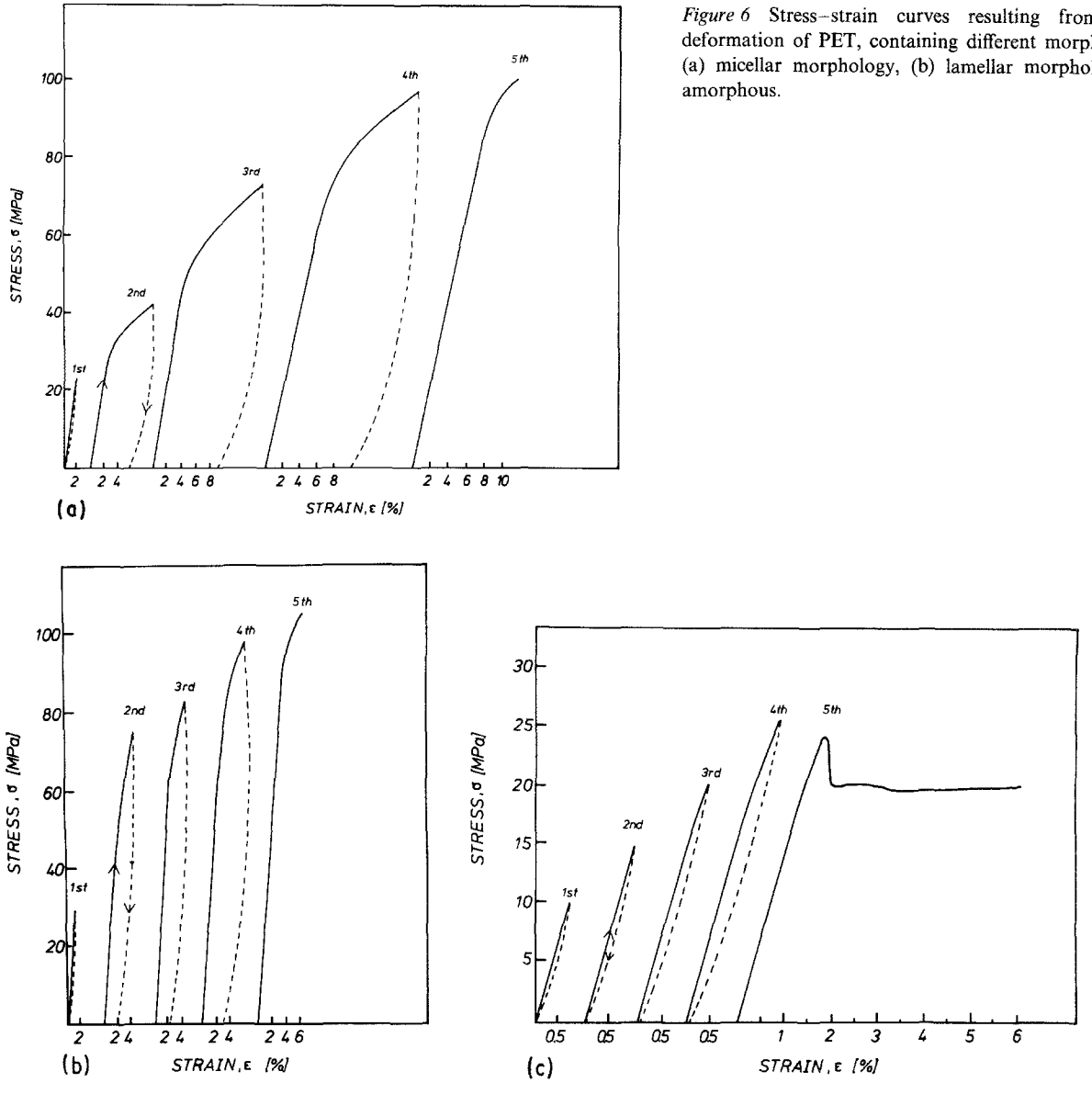

Figure 6 Stress–strain curves resulting from cyclic deformation of PET, containing different morphologies: (a) micellar morphology, (b) lamellar morphology, (c) amorphous.

where τ = shear stress in the fibre/matrix interface, G_m = shear modulus of the matrix, E_f = modulus of the fibre, r_0 = radius of the fibre, R = distance between two parallel fibres, A_f = cross-section area of the fibre, x = distance from one end of the longer needle crystal (Fig. 7) and l = length of longer crystal.

The short crystal is located in a gradient of shear stress and hence is exposed to a driving force. If the shear stress exceeds the yield stress of the matrix, the short needle will be displaced via plastic deformation of the matrix in the direction of the end of the long needle crystal. Reaching this point the shear gradient is zero and consequently no further migration of the short needle crystal occurs. With increasing overall strain, short crystals which are further from the ends

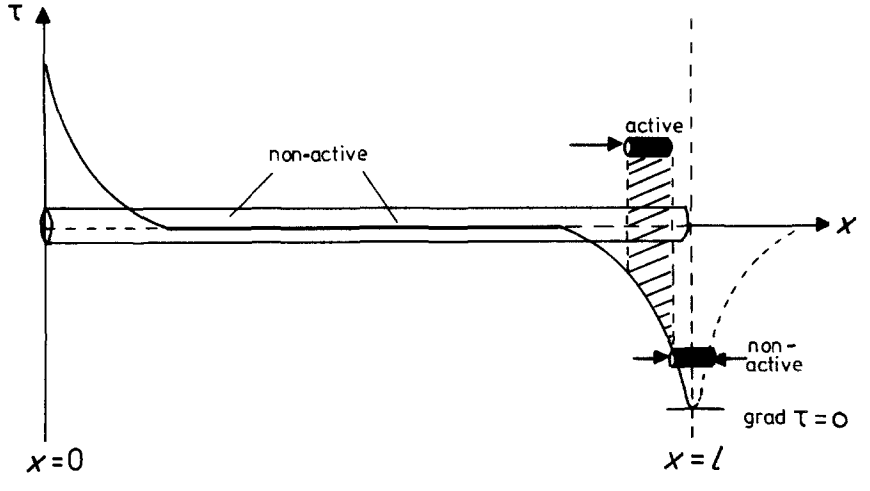

Figure 7 Schematic sketch, demonstrating the influence of the shear stress distribution on a small particle as a function of its position relative to the long fibre. Plastic displacement of the small particle occurs only in regions with grad $\tau \neq 0$.

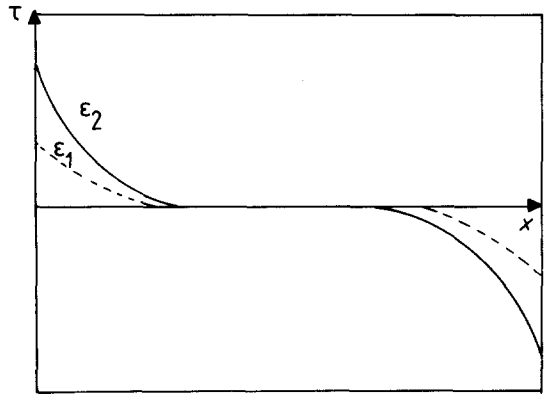

Figure 8 Shear stress distribution along a fibre of length l. Parameter is the strain, ε; $\varepsilon_2 > \varepsilon_1$.

of the long needle crystals may reach the critical driving force and will be displaced towards the needle ends. Expressing this in terms of a cyclic experiment, the overall strain of the first cycle has to be exceeded during the following one in order to displace the short crystals lying further away. Due to this fact an increase of the yield strain will be the consequence (Fig. 9). After repeated straining, all needle end-faces lie in a plane perpendicular to the orientation direction and no further driving force exists. This is the case for a lamellar arrangement of the polymer crystals. Only the linear elastic part is then observed (having a brittle amorphous matrix as in the case of 200° C annealed PET), Fig. 6b.

In the model used here, only the ends of the needle crystals are considered to be active (having sufficient shear gradient). With increasing length of the shorter needle crystals, the critical gradient for displacing them towards the ends of the longer needles must increase for two reasons: the number of sufficiently small crystals available to be displaced has decreased, and a higher gradient is needed to displace the somewhat "longer" short needle crystals, resulting in a steeper slope of the second part of the stress–strain curves.

The model proposed here should also be true for a system of discontinuous-fibre reinforced material, in which the matrix contains rigid short particles, but no such investigations are known to our knowledge.

5. Conclusions

The present report is concerned with the deformation behaviour of polymers with different crystalline morphologies. Summarizing the results obtained by cyclic deformation of the materials leads to the following conclusions:

1. Fibre self-reinforced polymers exhibit a second linear (plastic) part (when the Hookeian range is exceeded) with a slope $\alpha = d\sigma/d\varepsilon$, depending strongly on the apparent needle crystal length.

2. The deformation model includes two assumptions:
(a) a very broad distribution of needle crystal length, and
(b) the validity of the shear-lag model. The deformation mechanism is then described as a displacement of short needle crystals via plastic deformation of the matrix, with the shear stress gradient of a long needle crystal being the driving force.

3. Increasing overall strain leads to increasing yield strain, obtained at each new deformation cycle, while an increased shear stress gradient results in a steeper slope α.

Acknowledgement

We wish to thank Professor Dr H. G. Zachmann for many helpful discussions and the interest he focused on this work. We are also indebted to the Electron Microscope Centre of the TUHH for helpful assistance in the TEM investigations.

References

1. A. J. PENNINGS, *Macromol. Chem. Suppl.* **2** (1979) 99.
2. A. KELLER and J. A. ODELL, *J. Polym. Sci., Polym. Symp.* **63** (1978) 155.
3. J. PETERMANN, R. M. GOHIL, M. MASSUD and D. GÖRITZ, *J. Mater. Sci.* **17** (1982) 100.
4. P. SMITH and P. J. LEMSTRA, *Macromol. Chem.* **180** (1979) 591.
5. A. KARBACH, PhD thesis, Technical University Hamburg–Harburg (1986).
6. R. M. GOHIL and J. PETERMANN, *J. Mater. Sci.* **18** (1983) 1719.

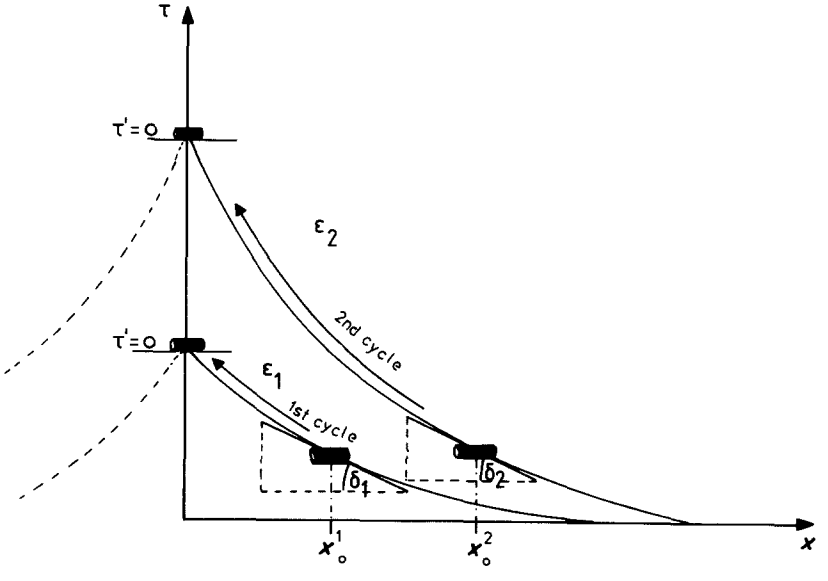

Figure 9 Enlarged section of two shear stress distributions with different gradients. The indicated short fibre is shifted in the direction of increasing gradient. In the second cycle a larger overall strain ε_2 is needed to obtain the same grad τ at the position x_0^2 compared to ε_1 and x_0^1. $\varepsilon_2 > \varepsilon_1$; $\delta_2 = \delta_1$; $x_0^2 > x_0^1$.

7. J. PETERMANN and R. M. GOHIL, *ibid.* **14** (1979) 2260.
8. R. M. GOHIL and J. PETERMANN, *J. Macromol. Sci. Phys.* **B18** (2) (1980) 217.
9. K. WENDEROTH, A. KARBACH and J. PETERMANN, *Colloid Polym. Sci.* **263** (1985) 301.
10. J. PETERMANN and U. RIECK, *J. Polym. Sci. Phys. Edn.* in press.
11. A. KELLY and H. LILHOLT, *Phil. Mag.* **20** (1969) 311.
12. W. H. SUTTON, B. W. ROSEN and D. G. FLOM, *Soc. of Petroleum Eng. J.* **20** (1964) 1.
13. W. H. BOWYER and M BADER, *J. Mater. Sci.* **7** (1972) 1315.
14. A. H. COTTRELL, *Proc. R. Soc.* **A282** (1984) 2.
15. B. O. OUTWATER, *Mod. Plast.* **33** (1956) 156.
16. A. KELLY, "Strong Solids" (Clarendon Press, Oxford, 1966) Ch. 5.

Received 12 May
and accepted 23 July 1986